symmetry

MDPI

Article

Structural Properties and Biological Prediction of ({[(1*E*)-3-(1*H*-Imidazol-1-yl)-1-phenylpropylidene] amino}oxy)(4-methylphenyl)methanone: An *In Silico* Approach

Maha S. Almutairi [1], Devarasu Manimaran [2], Issac Hubert Joe [2,*], Ola A. Saleh [3] and Mohamed I. Attia [1,3,*]

Received: 24 October 2015; Accepted: 16 December 2015; Published: 28 December 2015
Academic Editor: Soren Toxvaerd

[1] Department of Pharmaceutical Chemistry, College of Pharmacy, King Saud University, P.O. Box 2457, Riyadh 11451, Saudi Arabia; malmutbiri@ksu.edu.sa
[2] Centre for Molecular and Biophysics Research, Department of Physics, Mar Ivanios College, Thiruvananthapuram 695015, Kerala, India; manimaran.com@gmail.com
[3] Medicinal and Pharmaceutical Chemistry Department, Pharmaceutical and Drug Industries Research Division, National Research Centre, Dokki, Giza 12622, Egypt; ola.ahmedsaleh@yahoo.com
* Correspondence: hubertjoe@gmail.com (I.H.J.); mattia@ksu.edu.sa (M.I.A.)

Abstract: Bioactive molecules are playing essential role in the field of drug discovery and various pharmaceutical applications. Vibrational spectral investigations of the anti-*Candida* agent ({[(1*E*)-3-(1*H*-imidazol-1-yl)-1-phenylpropylidene]amino}oxy)(4-methylphenyl)methanone ((1*E*)-IPMM) have been recorded and analyzed to understand its structural geometry, inter- and intra-molecular interactions. The equilibrium geometry, harmonic vibrational wavenumber, natural bond orbital (NBO) and Frontier orbital energy analyses have been carried out with the help of density functional theory with B3LYP/6-311++G(d,p) level of theory. The detailed vibrational assignments for the title molecule were performed on the basis of potential energy distribution analysis in order to unambiguously predict its modes. The calculated wavenumbers had good agreement with the experimental values. NBO analysis has confirmed the intramolecular charge transfer interactions. The predicted docking binding energy gave insight into the possible biological activity of the title molecule.

Keywords: anti-*Candida*; FT-IR; FT-Raman; DFT/B3LYP; molecular docking

1. Introduction

Fungi are eukaryotic organisms and some of them are important human pathogens causing diseases such as aspergillosis, candidiasis and cryptococcosis. Actually, the incidence of severe fungal infections has increased in an alarming way over the past few decades. An antifungal drug is an agent that selectively attacks fungal pathogens with minimal toxicity to the host. Azoles are nitrogen-containing five-member heterocyclic ring system. They constitute the largest family of antifungal drugs and have been and are still widely used to treat superficial mucosal as well as deep and disseminated fungal infections. However, their extensive use gives rise to the development of resistance and resulted in therapeutic failure [1]. Azole antifungal agents inhibit biosynthesis of cell membrane sterols [2,3]. Single crystal X-ray structure and anti-*Candida* activity (minimum inhibitory concentration value = 0.3752 µmol/mL toward *Candida albicans*) of the titled azole-containing molecule, namely ({[(1*E*)-3-(1*H*-imidazol-1-yl)-1-phenylpropylidene]amino}oxy)(4-methylphenyl)methanone ((1*E*)-IPMM) were previously reported [4,5].

The present work deals with the FT-IR and FT-Raman spectral investigations of (1*E*)-IPMM to understand its structural geometry, inter- and intra-molecular interactions, hydrogen bonding, highest occupied molecular orbital-lowest unoccupied molecular orbital (HOMO–LUMO) energy and the natural bond orbital (NBO) analysis with the aid by density functional theory (DFT) calculations. The work also explores the biological activity of the title molecule by molecular docking approach.

2. Experimental

2.1. General

Melting point was performed using Gallenkamp melting point device, and it is uncorrected. Crystallographic data have been deposited with the Cambridge Crystallographic Data Center (supplementary publication number CCDC-1006859).

2.2. Synthesis

A solution containing *N*-(3-dimethylaminopropyl)-*N*′-ethylcarbodiimide hydrochloride (EDCI· HCl, 7.3 mmol), 4-dimethylaminopyridine (DMAP, 400 mg), and 4-methylbenzoic acid (7 mmol) in dichloromethane (75 mL) was stirred at room temperature. (1*E*)-*N*-Hydroxy-3-(1*H*-imidazol-1-yl)-1-phenylpropan-1-imine (6.9 mmol) [5] was added to the stirred reaction mixture and stirring was continued for further 18 h at ambient temperature. The reaction blend was washed successively with water (2 × 20 mL), 10% $NaHCO_3$ solution (2 × 15 mL) and water (2 × 15 mL). The organic layer was separated, dried (Na_2SO_4) and evaporated under vacuum. The residue was crystallized from isopropanol to give pale yellow crystals of the title compound **3** (m.p. 398–400 K) which were suitable for X-ray analysis [4]. ^1H and ^{13}C NMR as well as the mass spectral data of the title compound **3** are consistent with the previously reported ones [5].

2.3. Spectroscopic Measurements

The Fourier transform infrared spectrum of (1*E*)-IPMM was recorded using a Perkin Elmer RXL Spectrometer (Waltham, MA, USA) in the region 4000–400 cm^{-1}, with samples in the KBr using pellet press method. The resolution of the spectrum is 2 cm^{-1}. The FT-Raman spectrum of sample in the solid phase was recorded in the range 3500–50 cm^{-1} using a Bruker RFS 100/S FT-Raman spectrophotometer (Ettlingen, Germany) with a 1064 nm Nd:YAG laser source of 100 mW power (Göttingen, Germany).

2.4. Quantum Chemical Calculations

The quantum chemical computations of (1*E*)-IPMM have been performed using Gaussian 09 Program Package [6] at the Becke3-Lee-Yang-Parr (B3LYP) level with standard 6-311++G(d,p) basis set [6]. An empirical uniform scaling factor of 0.9673 was used to offset the systematic errors caused by basis set incompleteness, neglect of electron correlation and vibrational anharmonicity [7,8]. The calculated Raman activities (S_i) have been converted to relative Raman intensities (I_i) using the following relationship derived from the intensity theory of Raman scattering [9,10].

$$I_i = \frac{f\,(v_0 - v_i)^2\,S_i}{v_i\left[1 - \exp\left(-\frac{hcv_i}{kT}\right)\right]} \tag{1}$$

where ν_0 is the exciting wavenumber, ν_i is the vibrational wavenumber of the *i*th normal mode, *h*, *c* and *k* are fundamental constants, and *f* is a suitably chosen common normalization factor for all peak intensities. The simulated IR and Raman spectra have been plotted using pure Lorentzian band shape with a bandwidth of full width half maximum (FWHM) of 10 cm^{-1}.

3. Results and Discussion

3.1. Synthesis

The title molecule **3** was prepared using the commercially available acetophenone as illustrated in Scheme 1.

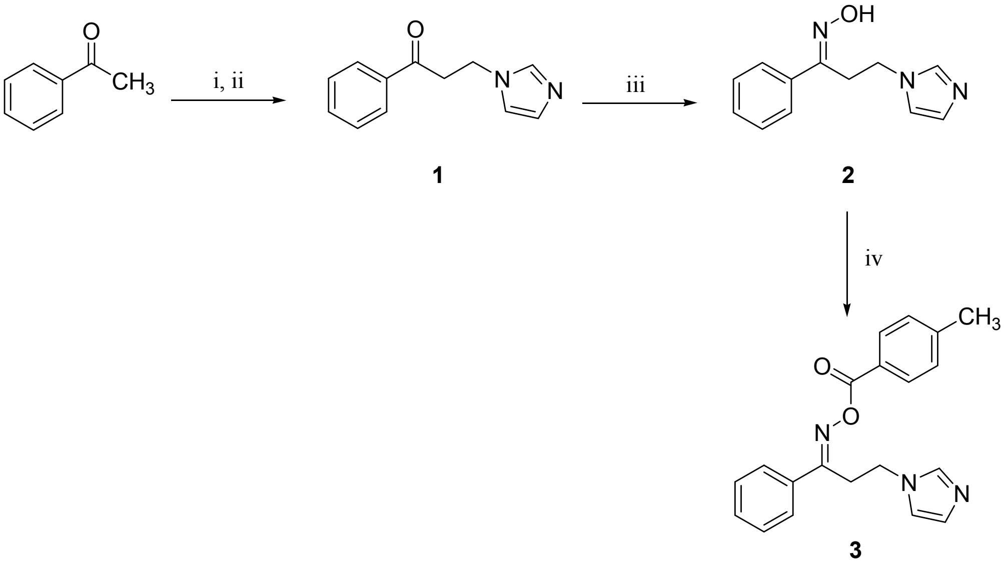

Scheme 1. Synthetic strategy to prepare the target molecule **3**. Reagents and conditions: (i) $HN(CH_3)_2 \cdot HCl$, $(CH_2O)_n$, conc. HCl, ethanol, reflux, 2 h; (ii) imidazole, water, reflux, 5 h; (iii) $H_2NOH \cdot HCl$, KOH, ethanol, reflux, 18 h; (iv) 4-methylbenzoic acid, EDCI· HCl, DMAP, DCM, rt, 18 h.

3.2. Structural Geometry Analysis

The optimized geometry of the molecule is determined by minimizing its energy with respect to all geometrical parameters without imposing molecular symmetry constraints. The optimized molecular structure of the isolated molecule is shown in Figure 1. The optimized bond lengths, bond and dihedral angles are presented in Table 1 in comparison with the experimental values. The calculated bond lengths of C16=O1, and C16–O2 are found to be 1.1993 Å and 1.3828 Å, respectively. The shortening of C16=O1 is due to the presence of double bond character. The calculated bond lengths of C–N bonds are C3–N21 (1.2859 Å), C36–N4 (1.4568 Å), C4–N39 (1.3817 Å), C4–N43 (1.3692 Å), C5–N41 (1.3757 Å), and C5–N43 (1.3131 Å) and the lengthening of the bond C36–N4 is due the conjugation effect of the imidazole moiety. The bond length of C39–H40 (1.0774 Å) is found to be shorter than the other C–H bonds, which is due to the presence of intra-molecular C–H$\cdots\pi$ bond interaction. In addition, the bond length of C33–C36 (1.5455 Å) appears to be longer than the other C–C bonds and it may be due to the charge transfer effect between the donor to acceptor group. The experimental and calculated value of bond length shows a good agreement in the correlation analysis (R^2 = 0.9945). The slight deviations in the bond angle and dihedral angles from the experimental XRD data are probably due to the intermolecular interactions in the crystalline state.

Table 1. The structural geometry parameters of (1*E*)-IPMM.

Bond Length (Å)			**Bond Angle (°)**			**Dihedral Angle (°)**		
Parameters	**Calculated**	**Experimental**	**Parameters**	**Calculated**	**Experimental**	**Parameters**	**Calculated**	**Experimental**
O1–C16	1.1993	1.1960	N3–O2–C16	113.03	112.71	C16–O2–N3–C21	−169.72	−174.61
O2–C16	1.3828	1.360	O2–N3–C21	111.26	108.99	N3–O2–C16–O1	9.74	4.71
O2–N3	1.4179	1.438	C36–N4–C39	127.25	127.11	N3–O2–C16–C15	−171.56	−175.29
N3–C21	1.2859	1.283	C36–N4–C43	126.44	126.39	O2–N3–C21–C22	−179.53	178.96
N4–C36	1.4568	1.456	C39–N4–C43	106.29	106.49	O2–N3–C21–C33	0.84	−0.30
N4–C39	1.3817	1.360	C41–N5–C43	105.23	104.26	C39–N4–C36–C33	−87.08	−87.21
N4–C43	1.3692	1.345	H7–C6–C8	120.88	119.87	C39–N4–C36–H37	152.42	151.25
N5–C41	1.3757	1.365	H7–C6–C15	118.76	119.79	C39–N4–C36–H38	36.49	34.35
N5–C43	1.3131	1.310	C8–C6–C15	120.36	120.35	C43–N4–C36–C33	90.66	94.49
C6–H7	1.0831	0.930	C6–C8–H9	119.42	119.36	C43–N4–C36–H37	−29.84	−27.05
C8–H9	1.0852	0.930	C6–C8–C10	121.1	121.28	C43–N4–C36–H38	−145.77	−143.95
C11–H12	1.0851	0.930	H9–C8–C10	119.48	119.36	C36–N4–C39–H40	−1.95	1.61
C13–H14	1.0818	0.929	C8–C10–C11	118.14	117.89	C36–N4–C39–C41	178.18	−178.44
C17–H18	1.0926	0.960	C8–C10–C17	120.78	121.19	C43–N4–C39–H40	179.94	−179.82
C17–H19	1.0918	0.959	C11–C10–C17	121.08	120.92	C43–N4–C39–C41	0.07	0.13
C17–H20	1.0955	0.960	C10–C11–H12	119.44	119.22	C36–N4–C43–N5	−178.27	179.09
C23–H24	1.0825	0.930	C10–C11–C13	121.19	121.53	C36–N4–C43–H44	2.52	−0.95
C25–H26	1.0839	0.930	H12–C11–C13	119.37	119.26	C39–N4–C43–N5	−0.14	0.50
C27–H28	1.0841	0.930	C11–C13–H14	119.9	120.03	C39–N4–C43–H44	−179.35	−179.53
C29–H30	1.0841	0.930	C11–C13–C15	120.2	119.88	C43–N5–C41–C39	−0.1	0.97
C31–H32	1.0823	0.930	H14–C13–C15	119.89	120.10	C43–N5–C41–H42	−179.75	−179.11
C33–H34	1.0926	0.970	C6–C15–C13	119.02	119.02	C41–N5–C43–N4	0.15	−0.89
C33–H35	1.0887	0.970	C6–C15–C16	117.54	118.37	C41–N5–C43–H44	179.32	179.14
C36–H37	1.0924	0.970	C13–C15–C16	123.43	122.51	H7–C6–C8–H9	0.17	1.56
C36–H38	1.0894	0.970	O1–C16–O2	123.93	123.87	H7–C6–C8–C10	−179.63	−178.47
C39–H40	1.0774	0.930	O1–C16–C15	125.36	125.55	C15–C6–C8–H9	179.86	−178.43
C41–H42	1.0788	0.931	O2–C16–C15	110.69	110.58	C15–C6–C8–C10	0.05	1.55
C43–H44	1.0806	0.930	C10–C17–H18	111.36	109.45	H7–C6–C15–C13	179.4	−179.42
C6–C8	1.3879	1.377	C10–C17–H19	111.49	109.47	H7–C6–C15–C16	0.28	3.90
C6–C15	1.4004	1.388	C10–C17–H20	110.72	109.44	C8–C6–C15–C13	−0.29	0.56
C8–C10	1.4013	1.388	H18–C17–H19	108.26	109.44	C8–C6–C15–C16	−179.41	−176.12
C10–C11	1.3993	1.388	H18–C17–H20	107.27	109.53	C6–C8–C10–C11	0.3	−1.94

Table 1. *Cont.*

Bond Length (Å)			Bond Angle (°)			Dihedral Angle (°)		
Parameters	**Calculated**	**Experimental**	**Parameters**	**Calculated**	**Experimental**	**Parameters**	**Calculated**	**Experimental**
C10–C17	1.5079	1.508	H19–C17–H20	107.55	109.50	C6–C8–C10–C17	−178.79	178.36
C11–C13	1.3911	1.380	N3–C21–C22	114.73	114.19	H9–C8–C10–C11	−179.51	178.03
C13–C15	1.3993	1.391	N3–C21–C33	123.56	124.71	H9–C8–C10–C17	1.41	−1.67
C15–C16	1.4884	1.481	C22–C21–C33	121.72	121.09	C8–C10–C11–H12	179.25	−179.71
C21–C22	1.4883	1.487	C21–C22–C23	121.7	121.76	C8–C10–C11–C13	−0.42	0.26
C21–C33	1.5146	1.503	C21–C22–C31	119.81	119.94	C17–C10–C11–H12	−1.66	−0.01
C22–C23	1.4012	1.390	C23–C22–C31	118.48	118.29	C17–C10–C11–C13	178.67	179.96
C22–C31	1.406	1.392	C22–C23–H24	120.8	119.69	C8–C10–C17–H18	−38.01	−39.32
C23–C25	1.3936	1.383	C22–C23–C25	120.73	120.50	C8–C10–C17–H19	−159.05	−159.26
C25–C27	1.3913	1.367	H24–C23–C25	118.46	119.82	C8–C10–C17–H20	81.25	80.72
C27–C29	1.396	1.377	C23–C25–H26	119.55	119.69	C11–C10–C17–H18	142.93	140.99
C29–C31	1.3883	1.378	C23–C25–C27	120.24	120.60	C11–C10–C17–H19	21.89	21.05
C33–C36	1.5455	1.520	H26–C25–C27	120.21	119.72	C11–C10–C17–H20	−97.81	−98.97
C39–C41	1.3711	1.348	C25–C27–H28	120.19	120.26	C10–C11–C13–H14	179.38	−178.19
			C25–C27–C29	119.56	119.52	C10–C11–C13–C15	0.18	1.81
			H28–C27–C29	120.25	120.22	H12–C11–C13–H14	−0.29	1.78
			C27–C29–H30	120.07	119.71	H12–C11–C13–C15	−179.49	−178.22
			C27–C29–C31	120.36	120.61	C11–C13–C15–C6	0.17	−2.21
			H30–C29–C31	119.57	119.61	C11–C13–C15–C16	179.24	174.32
			C22–C31–C29	120.63	120.48	H14–C13–C15–C6	−179.02	177.8
			C22–C31–H32	118.98	119.79	H14–C13–C15–C16	0.05	−5.67
			C29–C31–H32	120.38	119.74	C6–C15–C16–O1	6.16	12.52
			C21–C33–H34	108.61	108.90	C6–C15–C16–O2	−172.53	−167.47
			C21–C33–H35	110.58	108.89	C13–C15–C16–O1	−172.92	−164.03
			C21–C33–C36	113.79	113.42	C13–C15–C16–O2	8.39	15.97
			H34–C33–H35	107.62	107.70	N3–C21–C22–C23	156.34	150.54
			H34–C33–C36	107.5	108.89	N3–C21–C22–C31	−22.63	−28.46
			H35–C33–C36	108.53	108.89	C33–C21–C22–C23	−24.03	−30.17
			N4–C36–C33	114.24	114.07	C33–C21–C22–C31	157	150.83
			N4–C36–H37	107.49	108.76	N3–C21–C33–H34	−45.52	−45.77
			N4–C36–H38	108.62	108.77	N3–C21–C33–H35	−163.4	−162.95
			C33–C36–H37	108.55	108.73	N3–C21–C33–C36	74.16	75.65
			C33–C36–H38	110.28	108.73	C22–C21–C33–H34	134.88	135.02
			H37–C36–H38	107.42	107.59	C22–C21–C33–H35	17	17.84
			N4–C39–H40	121.91	127.03	C22–C21–C33–C36	−105.44	−103.57

Table 1. *Cont.*

Bond Length (Å)			Bond Angle (°)			Dihedral Angle (°)		
Parameters	**Calculated**	**Experimental**	**Parameters**	**Calculated**	**Experimental**	**Parameters**	**Calculated**	**Experimental**
			N4–C39–C41	105.71	105.95	C21–C22–C23–H24	0.24	1.07
			H40–C39–C41	132.38	127.02	C21–C22–C23–C25	−178.79	−178.91
			N5–C41–C39	110.5	110.84	C31–C22–C23–H24	179.23	−179.92
			N5–C41–H42	121.55	124.57	C31–C22–C23–C25	0.19	0.10
			C39–C41–H42	127.94	124.59	C21–C22–C31–C29	179.08	178.81
			N4–C43–N5	112.27	112.45	C21–C22–C31–H32	−1.07	−1.18
			N4–C43–H44	121.89	123.80	C23–C22–C31–C29	0.07	−0.22
			N5–C43–H44	125.84	123.75	C23–C22–C31–H32	179.92	179.79

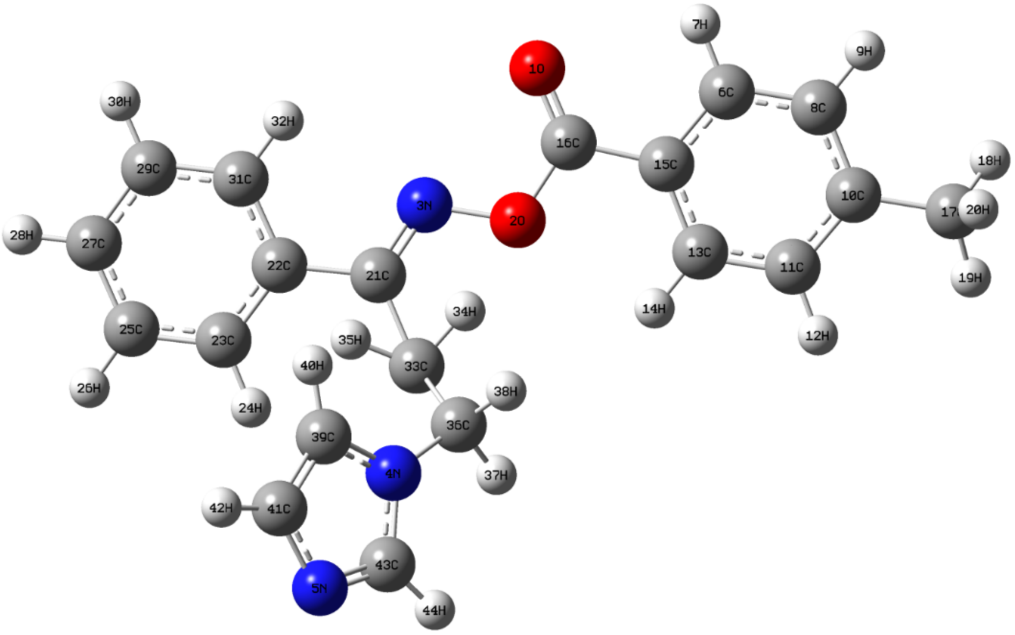

Figure 1. Optimized structure of (1E)-IPMM.

3.3. Natural Bond Orbital (NBO) Analysis

The natural bond orbital (NBO) calculations were performed using NBO 3.1 program as implemented in the Gaussian 09 package [6] at the DFT level [11]. The corresponding results have been presented in Table 2. A useful aspect of the NBO method is that it gives information about interactions in both filled and virtual orbital spaces, which could enhance the analysis of intra-and intermolecular interactions that will give a measure of the intermolecular delocalization or hyper conjugation. Delocalization of electron density between occupied Lewis-type (bond or lone pair) NBO orbital and formally unoccupied (anti-bond or Rydberg) non-Lewis NBO orbital corresponds to a stabilizing donor-acceptor interaction. The delocalization effect can be described as a charge transfer from the highest occupied bonding orbital into unoccupied anti bonding orbital and their importance can be more quantitatively characterized through a second order perturbative treatment that gives the energy lowering associated with such interaction. The magnitude of these delocalization effects can be determined from an analysis of the off diagonal elements in the Fock matrix of the NBO basis by taking into account all possible donor-acceptor interactions. The hyper conjugative interaction energy was deduced from the second-order perturbation approach as

$$E\,(2) = -n_{\sigma}\frac{<\sigma|F|\sigma>^{2}}{\varepsilon_{\sigma *}-\varepsilon_{\sigma}} = -n_{\sigma}\frac{{F_{ij}}^{2}}{\Delta E} \tag{2}$$

where $<\sigma\,|\,F\,|\,\sigma>^2$ or ${F_{ij}}^2$ is the Fock matrix element between i and j NBO orbital, ε_{σ} and $\varepsilon_{\sigma *}$ are the energies of σ and σ* NBO's, and n_{σ} is the population of the donor σ orbital [12]. The larger value of hyperconjugative interaction energy (E(2)) implies that the interaction between electron donors and electron acceptors is more intensive and thus the greater the extent of the conjugation of the whole system. Here, the intra-molecular hyperconjugative interactions are formed by the orbital overlap between π(C–C) and π*(C–C) bond orbital which results in intramolecular charge transfer (ICT), causing stabilization of the system. These interactions are observed as an increase in electron density (ED) in C–C anti bonding orbital that weakens the respective bonds. The ED value of the phenyl rings (∼1.6e) shows strong charge delocalization. However, the two conjugated π bonds (∼1.8e) and π* bonds (∼0.3e) of the imidazole ring clearly demonstrate a lesser degree of conjugation leading to dearomatization. The important interactions between filled (donors) Lewis type NBO and empty (acceptors) non Lewis NBOs are reported. The most important interaction (n-π^*) and (n-σ^*) energies of LP1N4 → π^*(N5–C43) and LP2O1 → σ^*(O2–C16) are 45.86 and 37.90 kcal/mol, respectively. This larger E(2) value reveals the strong ICT interactions of this molecule.

Table 2. Second order perturbation theory analysis of Fock matrix in natural bond orbital (NBO) basis for (1*E*)-IPMM.

Donor (*i*)	**ED (*e*)**	**Acceptor (*j*)**	**ED (*e*)**	**E(2) [a] (kcal/mol)**	**$E(i)$–$E(j)$ [b] (kcal/mol)**	**$F(i,j)$ [c] (kcal/mol)**
π(N5–C43)	1.8696	π^*(C39–C41)	0.2991	20.96	0.33	0.077
π(C6–C8)	1.6612	π^*(C10–C11)	0.3353	22.79	0.29	0.072
π(C6–C8)	1.6612	π^*(C13–C15)	0.3800	18.34	0.28	0.065
π(C10–C11)	1.6285	π^*(C6–C8)	0.2882	17.02	0.28	0.063
π(C10–C11)	1.6285	π^*(C13–C15)	0.3800	24.38	0.28	0.074
π(C13–C15)	1.6473	π^*(O1–C16)	0.2324	20.53	0.27	0.069
π(C13–C15)	1.6473	π^*(C6–C8)	0.2882	20.63	0.29	0.070
π(C13–C15)	1.6473	π^*(C10–C11)	0.3353	17.40	0.29	0.064
π(C22–C23)	1.6487	π^*(N3–C21)	0.1570	15.73	0.27	0.061
π(C22–C23)	1.6487	π^*(C25–C27)	0.3192	19.10	0.29	0.066
π(C22–C23)	1.6487	π^*(C29–C31)	0.2875	18.74	0.29	0.067
π(C25–C27)	1.6565	π^*(C22–C23)	0.3739	21.13	0.28	0.069
π(C25–C27)	1.6565	π^*(C29–C31)	0.2875	18.43	0.29	0.066
π(C29–C31)	1.6602	π^*(C22–C23)	0.3739	19.73	0.28	0.067
π(C29–C31)	1.6602	π^*(C25–C27)	0.3192	20.94	0.28	0.069
π(C39–C41)	1.8516	π^*(N5–C43)	0.3813	15.41	0.27	0.062
LP(2) O1	1.8315	σ^*(O2–C16)	0.1184	37.90	0.57	0.133
LP(2) O1	1.8315	σ^*(C15–C16)	0.0639	17.29	0.69	0.100
LP(2) O2	1.7979	π^*(O1–C16)	0.2324	35.59	0.36	0.102
LP(2) O2	1.7979	π^*(N3–C21)	0.1570	12.38	0.36	0.060
LP(1) N4	1.5610	π^*(N5–C43)	0.3813	45.86	0.28	0.102
LP(1) N4	1.5610	π^*(C39–C41)	0.2991	30.46	0.29	0.088
LP(1) O2	1.9728	π^*(C33–H35)	0.0128	0.72	1.04	0.025

[a] E(2) means energy of hyperconjugative interactions; Equation (2); [b] Energy difference between donor and acceptor i and j NBO orbitals; [c] $F(i,j)$ is the Fock matrix element between i and j NBO orbitals.

3.4. Vibrational Spectral Analysis

The FT-IR and FT-Raman spectra of (1*E*)-IPMM have been analyzed on the basis of density functional theory calculations. The vibrational modes were assigned on the basis of potential energy distribution (PED) analysis using the VEDA 4 program [13]. The combined experimental and simulated Infrared and Raman spectra are shown in Figures 2 and 3 respectively. The computed wavenumbers are compared with the experimental FT-IR and FT-Raman wavenumbers and their assignments are presented in Table 3. Vibrational analysis is based on the vibrational modes of the groups phenyl ring, methylene, methyl, imidazole ring and skeletal mode.

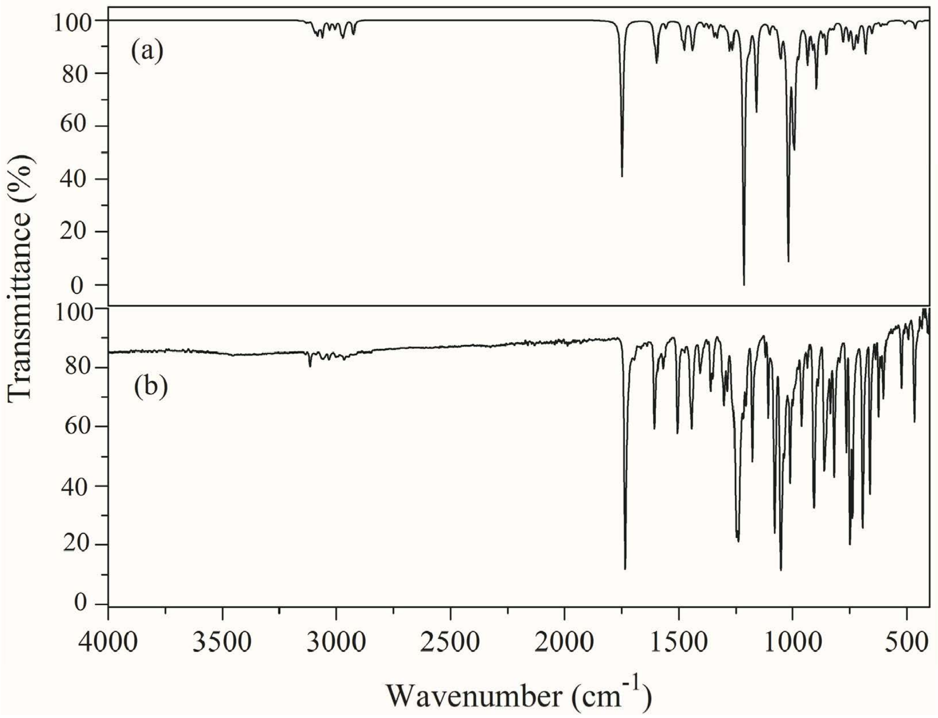

Figure 2. (**a**) Simulated (**b**) Experimental FT-IR spectrum of (1*E*)-IPMM.

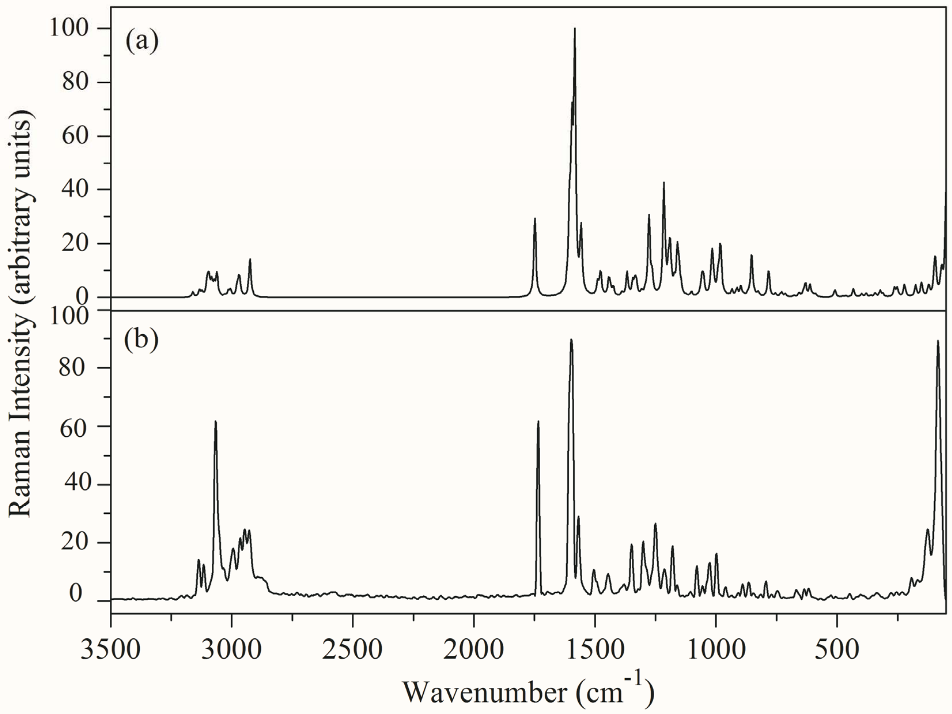

Figure 3. (**a**) Simulated (**b**) Experimental FT-Raman spectrum of (1*E*)-IPMM.

Table 3. Vibrational assignment of (1*E*)-IPMM.

Calculated Wavenumber (cm^{-1})		Experimental Wavenumber (cm^{-1})		IR Intensity	Raman Intensity	Force Constant Mdyne/Å	Assignments with PED%
Unscaled	Scaled	IR	Raman				
3268	3161	–	–	0.593	0.39	6.9489	CH ss (85), CH ss (13)
3239	3134	–	3136 M	3.6251	0.51	6.7536	CH as (85), CH as (14)
3228	3123	–	–	2.2934	0.35	6.7270	CH v (98)
3208	3103	3116 VW	3116 M	4.7262	0.67	6.6208	CH ss (96)
3205	3100	–	–	2.7163	0.64	6.6210	CH ss (88)
3200	3095	–	–	3.2974	0.55	6.5918	CH ss (95)
3198	3094	–	–	11.246	0.8	6.5894	CH ss (69), CH ss (21)
3187	3083	–	–	21.7901	1.12	6.5450	CH as (50), CH as (18)
3177	3073	–	–	7.1817	0.83	6.4757	CH as (45), CH as (44)
3166	3063	–	3066 S	0.2433	0.31	6.4132	CH as (44), CH as (28), CH as (25)
3165	3061	–	–	13.691	0.67	6.4307	CH ss (77), CH ss (18)
3164	3060	3058 VW	–	12.943	0.83	6.4245	CH as (77), CH as (19)
3132	3029	3032 VW	–	14.3723	0.1	6.3489	CH ss (52), CH ss (33)
3116	3014	–	–	2.0283	0.42	6.3011	CH ss (47), CH ss (31), CH ss (13)
3107	3005	3001 VW	2994 M	13.465	0.53	6.2686	CH as (62), CH as (36)
3079	2978	–	–	16.7718	0.78	6.1126	CH as (43), CH as (37), CH as (20)
3070	2969	2965 VW	2965 M	23.7511	1.58	5.9039	CH ss (49), CH ss (30), CH ss (11), CH ss (10)
3061	2961	2945 VW	–	7.8155	0.15	5.8801	CH as (51), CH ss (35)
3024	2925	–	2928 M	24.0513	3.15	5.6052	CH ss (62), CH ss (20), CH ss (17)

Table 3. *Cont.*

Calculated Wavenumber (cm^{-1})		Experimental Wavenumber (cm^{-1})		IR Intensity	Raman Intensity	Force Constant Mdyne/Å	Assignments with PED%
Unscaled	Scaled	IR	Raman				
			2893 W 2878 W 2858 W				Overtones and Combination bands
1807	1748	1735 VS	1735 S	269.1274	6.69	25.0634	O=C ss (88)
1660	1605	1604 M	–	26.7859	6.42	14.4429	vN=C (60)
1649	1595	–	1597 VS	64.4175	11.64	9.3552	vCC (22), vCC (17)
1637	1584	–	–	6.3303	20.09	8.9281	vCC (28), vCC (16)
1610	1558	1569 VW	1568 M	8.6839	4.96	8.1884	vNC (13), vCC (20), vCC (15), vCC (11)
1608	1555	–	–	3.9604	0.32	9.0692	vCC (32)
1539	1489	1505 M	1505 W	1.8657	1.04	3.4994	δCCH (18), δCCH (17), δCCH (16)
1536	1486	–	–	22.6513	0.13	5.3525	vN=C (33), vC=C (33), δCCH (13)
1527	1477	–	–	2.8843	1.4	2.9785	δCCH (14), δCCH (13)
1526	1476	–	–	42.0124	0.54	3.0799	vC=C (13), CH2sci (19)
1493	1444	1443 M	1446 W	13.357	0.9	1.4623	CH3sci (41), CH3sci (26)
1489	1441	–	–	18.9506	0.28	1.6996	CH2sci (51), δCH2 (47)
1488	1440	–	–	10.9672	0.46	1.3911	CH3sci(38)
1483	1435	–	–	23.2028	0.29	1.5608	CH2sci (61)
1472	1424	1407 W	–	2.639	0.7	2.5501	δsCCH (24), vCC (13)
1436	1389	–	1380 W	8.6605	0.28	3.0566	vCC (20), δCCH (12)
1414	1367	–	–	7.3558	0.25	2.0790	NCHtwi (32)
1414	1367	1360 W	–	2.2648	1.73	1.6400	δsCH3 (22),δCH2 (13)

Table 3. *Cont.*

Calculated Wavenumber (cm^{-1})		Experimental Wavenumber (cm^{-1})		IR Intensity	Raman Intensity	Force Constant Mdyne/Å	Assignments with PED%
Unscaled	**Scaled**	**IR**	**Raman**				
1390	1344	–	1349 M	21.4422	1.09	2.4537	vNC (15), CH2wag (15)
1381	1336	–	–	3.75	0.78	2.5704	vNC (27), CH2wag (19)
1375	1330	–	–	23.9291	1.13	1.8331	δCCH (10)
1351	1307	1302 W	1301 M	5.575	0.35	1.9302	vCC (12), δsCCH (20)
1337	1293	–	–	5.0344	0.05	6.1367	vCC (31), vCC (27)
1334	1291	–	–	2.0028	0.24	1.4769	δsCCH (22)
1326	1283	1286 W	–	0.9504	0.14	3.7665	vCC (24)
1320	1277	–	–	41.0481	6.55	2.2416	vCC (26), δCCH (17)
1307	1265	–	1250 M	37.7926	1.46	1.9430	δsCCH (35), vNC (12)
1259	1218	1238 S	–	65.5138	0.34	1.5270	δNCH (55), vNC (10)
1256	1215	1206 W	–	394.8687	8.95	3.0905	vCC (33), δCCH (12)
1237	1197	–	–	16.8257	1.9	1.4384	δCCH (33)
1230	1189	–	–	27.0607	3.94	3.2248	vCC (39), δCCC (12)
1212	1173	1177 M	1180 M	2.3703	0.97	0.9970	vCC (11), δsCCH (20)
1199	1160	–	1161 W	148.5022	3.52	1.0149	δsCCH (20)
1193	1154	–	–	1	1.51	1.1323	vNC (11), δNCH (14)
1185	1146	–	–	0.1824	0.74	0.9300	δsCCH (33)
1140	1103	1107 W	1106 VW	1.9151	0.07	1.0086	vCC (19), δsCCH (20)
1138	1101	–	–	17.4222	0.25	1.5829	vNC (62), δsCCH (20)
1113	1077	1078 S	–	5.3066	0.03	1.1960	vCC (20), δsCCH (15)
1095	1059	–	–	27.4394	1.54	1.0008	vCC (19), δsCCH (46)
1087	1052	1051 VS	1056 M	42.9985	1.43	1.8490	–
1060	1025	–	1026 M	10.928	0.07	1.0692	δasCCH (62)
1054	1020	–	–	382.4008	1.22	1.9040	vOC (24)
1050	1015	–	–	16.3115	2.41	1.7360	vCC (27)
1046	1012	1010 M	–	14.8755	1	2.0414	vNC (20), δsCCN (31)
1032	998	–	998 M	119.1442	0.1	2.0580	δsCCC (24)
1025	992	–	–	150.1159	1.56	1.7637	vCC (15)
1015	982	–	–	10.5957	4.12	3.5570	vCC (14), δsCCC (27)
1010	977	–	–	0.2509	0.09	0.7885	HCCHtwi (47)
1006	973	–	–	39.6089	0.16	0.8858	δsCH3 (55)
1001	968	–	–	0.7333	0.01	0.8021	HCCHtwi (80)

Table 3. *Cont.*

Calculated Wavenumber (cm^{-1})		Experimental Wavenumber (cm^{-1})		IR Intensity	Raman Intensity	Force Constant Mdyne/Å	Assignments with PED%
Unscaled	Scaled	IR	Raman				
991	959	960 W	961 W	0.145	0.08	0.7930	HCCHtwi (40)
980	948	–	–	3.9185	0.04	0.7761	δasCCCH (54)
966	934	935W	–	66.3139	0.53	2.0584	vCC (36)
945	914	–	–	33.2026	0.63	0.9804	HCCHtwi (24)
928	897	906 M	–	111.0668	0.83	1.0686	vON (17), HCCHtwi (15)
917	887	–	890 W	5.8457	0.1	3.1525	δsCNC (70)
899	870	863 M	865 W	18.2761	0.18	1.8980	vCC (12), vON (13)
882	853	–	–	53.555	3.69	2.6957	vON (22)
869	841	–	–	1.649	0.15	0.6090	HCCHtwi (80)
861	832	835 W	–	8.1045	0.01	0.6028	CCCHopb (79)
854	826	–	–	1.9587	0.31	0.5388	HCCHopb (50)
848	821	819 M	–	9.9934	0.04	0.6698	CCCHopb (50)
810	783	–	794 W	3.9159	2.27	1.8007	vCC (18), δCCC (30)
806	780	764 M	–	31.983	0.03	0.5309	NCCNopb (87)
781	755	749 S	–	28.9486	0.23	0.7004	CCCHopb (53)
761	736	737 S	–	33.4661	0.13	1.0165	CCCCopb (13), τOCCO (38)
753	729	–	–	30.0271	0.34	1.2388	vCC (15)
738	714	–	–	30.7013	0.22	0.3981	HCNCopb (76)
703	680	694 S	–	54.5898	0.01	0.5922	CCCCopb (39)
701	678	–	–	1.2881	0.09	0.8929	CCCCopb (19), τOCCO (16)
679	657	–	–	3.2453	0.31	1.2364	δCCC (14)
673	651	–	–	18.7772	0.01	0.9418	NCCNopb (89)
661	639	636 VW	636 VW	0.5431	0.36	1.0390	vNC (29), δCCN (13)
652	631	623 W	618 VW	2.8157	1.06	1.6943	δCCC (43)
635	614	–	–	5.4204	0.34	0.9863	CCNCopb (44), δCCC (15)
632	611	612 W	–	2.7071	0.68	1.1482	δCCC (34), τCCNC (25)
620	599	602 W	–	5.011	0.16	1.0360	δCCC (25), δCC=O (12)
609	589	–	–	5.5383	0.21	0.8308	NCCCopb (13)
526	509	525 W	–	5.7184	0.59	0.8315	CCNopb (12)
493	477	493 VW	–	1.2364	0.06	0.4729	CCCCopb (28)
479	464	466 W	–	13.7513	0.1	0.4369	CCCCopb (36)
			448 VW				

Table 3. *Cont.*

Calculated Wavenumber (cm^{-1})		Experimental Wavenumber (cm^{-1})		IR Intensity	Raman Intensity	Force Constant Mdyne/Å	Assignments with PED%
Unscaled	**Scaled**	**IR**	**Raman**				
447	433	434 VW	–	1.5492	0.7	0.5503	δCCC (20), δCCN (17)
416	403	404 VW	403 VW	0.0615	0	0.2964	CCCCopb (47)
412	398	–	–	0.1288	0.26	0.2902	CCCCopb (48)
393	380	–	–	2.3925	0.3	0.3513	δCCN (31)
372	360	–	–	1.3636	0.11	0.5099	vCC (14)
355	344	–	–	2.0459	0.21	0.1924	CH2opb (14), δCNC (29)
354	342	–	335 VW	2.8112	0.11	0.1949	CH2opb (37), δCNC (16)
333	322	–	–	1.1973	0.51	0.4237	CCCCopb (11), τCCNO (35)
322	311	–	–	2.7272	0.25	0.2073	CH2opb (28), δCNC (20)
272	263	–	–	3.6921	0.75	0.2031	CCCCopb (46)
260	252	–	–	2.0039	0.71	0.2151	CCCopb (31), δCON (22)
229	222	–	–	0.4991	1.01	0.0980	vOC (10), δCCC (10)
182	176	–	192 W	1.7133	0.95	0.0980	CNC=Nopb (19), δCCC (30)
157	152	–	–	0.9648	1.13	0.0804	CCCCopb (34)
126	122	–	125 M	1.9862	0.87	0.0521	δCCC (22), δCCO (17)
103	99	–	–	1.3736	0.72	0.0298	CCCCopb (26), δCNC=N (27)
98	95	–	83 VS	0.972	2.92	0.0174	δCNC=N (25), τCCCC (23)
71	69	–	–	1.0649	1.91	0.0174	CCNCopb (14), τCCCO (29)
52	50	–	–	1.6541	6.9	0.0070	CCNCopb (40), τCCCO (25)
46	45	–	–	0.1833	1.85	0.0064	δCON (25), δCCO (16)
38	37	–	–	0.9354	6.12	0.0034	τCCCO (28), τCCCN (15)
33	32	–	–	0.2588	2.81	0.0007	C-CH3opb (89)
27	26	–	–	1.8136	9.93	0.0023	CCCNopb (21)
26	25	–	–	0.0469	2.53	0.0017	(29), τCONC (29)
17	17	–	–	0.7348	35	0.0009	τCCCN (25),τCCON (18)
12	12	–	–	0.9577	41.04	0.0005	τCCON (44)

3.4.1. Phenyl Ring Vibrations

In general, aromatic C–H stretching vibrations absorbs in the region 3080–3010 cm^{-1} [14]. The intense Raman band is observed 3066 cm^{-1}, which corresponds to C–H stretching vibration. In addition, aromatic C=C stretching vibrations occurs in the region 1625–1430 cm^{-1} [15]. The intense band is observed at 1597 cm^{-1} in the Raman spectrum. The in-plane C–H deformation vibration generally appears in the region 1290–1000 cm^{-1}. The C–H out-of-plane deformation expected around 860–800 cm^{-1} [14]. A medium intense IR band is observed at 819 cm^{-1} in IR spectrum, which is calculated to be at 821 cm^{-1} with PED 50% can be attributed to C–H deformation mode.

3.4.2. Methylene Vibrations

The methylene symmetric vibrations expected around in the region 2865–2845 cm^{-1} [15]. The weak Raman band is observed at 2858 cm^{-1} can be attributed to CH_2 symmetric stretching mode. The –CH_2 in-plane vibration expected around in the region 1480–1440 cm^{-1} [14]. The methylene scissoring mode is observed at 1443 cm^{-1} (IR) and 1446 cm^{-1} (Raman). The –CH_2 wagging appears around 1411–1174 cm^{-1} [16]. The Raman band appearing at 1349 cm^{-1} is assigned to be methylene wagging vibration mode.

3.4.3. Methyl Vibrations

The methyl group asymmetric vibrations generally appear in the regions 2972–2952 cm^{-1}. The methyl asymmetric stretching band is observed at 2965 cm^{-1}, in both IR and Raman spectra. The methyl group symmetric bending modes expected to occur in the region 1365–1385 cm^{-1} [15]. The observed band at 1360 cm^{-1} in IR spectrum is calculated to be at 1367 cm^{-1} with PED 38% can be attributed to methyl bending modes.

3.4.4. Imidazole Ring Vibrations

The imidazole ring CH vibrations expected to occur at 3145–3115 cm^{-1} [14]. The medium Raman band is observed at 3136 cm^{-1} assigned to imidazole C–H stretching mode.

3.4.5. Skeletal Mode Vibrations

The C–N and C–C stretching vibrations generally arises in the region 1150–850 cm^{-1} [17–19]. The C–C and N–C stretching modes are observed at 1078 and 1010 cm^{-1}, respectively in the IR spectrum.

3.5. HOMO–LUMO Energy Analysis

The highest occupied molecular orbital (HOMO) energy characterizes the ability of electron giving, whereas the lowest unoccupied molecular orbital (LUMO) energy characterizes the ability of electron accepting. The energy difference between HOMO and LUMO orbitals is called as energy gap, which is an important stability factor for structures. They indicate the electron transport in molecular systems. It is worth noting that HOMOs have an overall π bonding character along with a considerable non-bonding character and LUMOs have an anti-bonding π^* character. The strong charge transfer interaction through π conjugated bridge results in substantial ground state donor-acceptor mixing and the appearance of a charge transfer band in the electronic absorption spectrum. Therefore, an electron density (ED) transfer occurs from the more aromatic part of the π conjugated system in the electron-donor side to its electron-withdrawing part. The HOMO-LUMO energy gap for (1*E*)-IPMM was computed at the B3LYP/6-311++G(d, p) level basis set. The HOMO of the title molecule is located on the imidazole ring and LUMO on phenyl rings. This indicates that the charge transfer between the imidazole ring to phenyl ring system is through the C=N bond. The Eigen values of LUMO (−2.02 eV) and HOMO (−6.36 eV) and their energy gap (4.34 eV), explains the eventual charge transfer interactions taking place within the molecule. The frontier molecular orbital diagrams are shown in Figure 4.

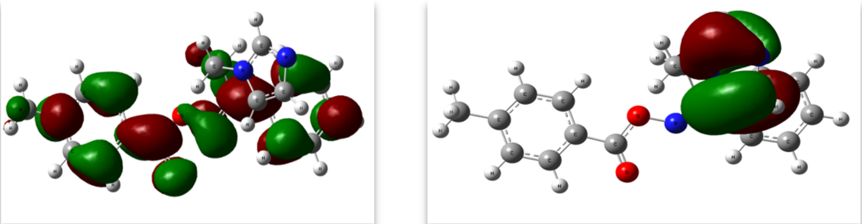

(**a**) (**b**)

Figure 4. (**a**) HOMO; (**b**) LUMO plots of (1*E*)-IPMM.

3.6. NMR Spectral Analysis

The scaled and experimental chemical shift values are presented in Table 4. The computed chemical shifts were scaled down by the linear regression method for neglecting the systematic errors [20–25]. The empirically scaling was carried out by following equation

$$\delta_{\text{calc}}^{\text{scaled}} = \frac{(\text{intercept} - \sigma)}{\text{slope}} \tag{3}$$

where σ is the calculated isotropic shielding value for a particular nucleus.

The phenyl ring carbon signals are observed at 125.80, 127.20, 144.64, 129.01, 129.54, 129.61, 130.09, 131.23 and 136.91 ppm. The two signals at 133.07 and 118.73 ppm are corresponding to the imidazole ring carbon atoms. Similarly, imidazole ring proton signals are observed at 6.84, 6.94 and 7.37 ppm. The methylene groups signals were observed at 31.04 and 43.65 ppm for carbons and at 3.36, 4.21 ppm for hydrogens. Their corresponding theoretical chemical shift values appeared at 30.68 and 44.04 ppm (^{13}C) and at 3.24 and 4.21 ppm (^{1}H) in NMR spectra. The ^{13}C spectrum showed a signal at 21.79 ppm for the methyl carbon, which is calculated to be 19.86 ppm. The predicted chemical shift values showed good agreement with the experimental results.

Table 4. The predicted and experimental NMR chemical shifts of (1*E*)-IPMM.

	^{13}C			^{1}H	
Atom	$\delta_{\text{exp.}}$	$\delta_{\text{cal.}}$	**Atom**	$\delta_{\text{exp.}}$	$\delta_{\text{cal.}}$
C6	131.23	131.08	H7	7.85	7.85
C8	129.01	128.71	H9	7.23	7.58
C10	144.64	146.91	H12	7.23	6.94
C11	129.01	127.70	H14	7.85	7.60
C13	129.54	128.47	H18	2.37	1.12
C15	125.80	125.88	H19	2.37	1.11
C16	163.17	162.04	H20	2.37	2.37
C17	21.79	19.86	H24	7.59	7.35
C21	163.48	164.41	H26	7.35	7.33
C22	136.91	135.25	H28	7.41	7.39
C23	129.61	126.13	H30	7.35	7.41
C25	130.09	127.30	H32	7.59	7.86
C27	131.23	130.22	H34	3.36	3.24
C29	130.09	128.05	H35	3.36	2.82
C31	129.61	126.99	H37	4.21	3.37
C33	31.04	30.68	H38	4.21	4.21
C36	43.65	44.04	H40	6.84	6.94
C39	118.73	119.84	H42	6.94	6.84
C41	127.20	128.46	H44	7.37	7.36
C43	133.07	135.83	–	–	–

3.7. Molecular Docking Analysis

The structure of (1*E*)-IPMM was optimized based on the density functional theory using Gaussian 09 program [6]. The molecular docking was performed using AutoDock Tools-1.5.4 interfaced with the MGL Tools-1.5.4 package [26]. The antifungal target protein of *Mycobacterium tuberculosis* Cyp51 (PDB ID: 1EA1) in complex with the standard antifungal drug fluconazole, was selected for the present docking analysis [27]. The three-dimensional (3D) coordinates of the protein file was downloaded from the Research Collaboratory for Structural Bioinformatics (RCSB) protein data bank [28], with a resolution of 2.21 Å. The protein preparation has been carried out by the following steps (i) all water molecules were removed (ii) hydrogen atoms were added to the crystal structure (iii) add Coulomb charges (iv) and previous docked inhibitor (fluconazole) was removed from the protein. The AutoGrid 4.2 [29,30] was used to create affinity grids centered on the active site with 126 × 126 × 126 grid size with a spacing of 0.42 Å. The rigid protein and flexible ligand dockings were performed by using AutoDock 4.2 with the Lamarckian genetic algorithm applying the following protocol: trials of 100 dockings, energy evaluations of 25,000,000, population size of 200, a mutation rate of 0.02, a crossover rate of 0.8, and an elitism value of 1. The docking results were evaluated by sorting the binding free energy predicted by docking confirmations. The predicted best confirmation binding energy was −7.15 kcal/mol. The amino acid ARG96 present in the active site of the target protein binds with the ligand by N–H$\cdots$N hydrogen bonding. The protein-ligand interaction complex is given in Figure 5 supporting the symmetry between the observed antifungal activity of (1*E*)-IPMM and docking results.

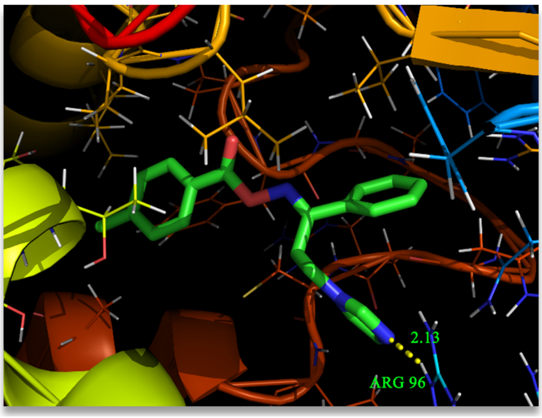

Figure 5. Binding pose of (1*E*)-IPMM with amino acid residues.

4. Conclusions

All DFT calculations of (1*E*)-IPMM have been performed at B3LYP/6-31++G(d,p) level basis set to predict the molecular geometry, vibrational wavenumbers and orbital energy analysis. The detailed vibrational assignments were unambiguously performed on the basis of PED analysis to predict the vibrational modes. The scaled wavenumbers are in a good agreement with the experimental results. The decrease in C–H bond length reveals the presence of intra-molecular C–H$\cdots\pi$ bond interaction. The NBO analysis also confirms the C–H$\cdots\pi$ interactions. The HOMO-LUMO energy reveals the occurrence of the charge transfer interactions within the molecule. The molecular docking results indicated that the title molecule is an effective antifungal agent capable of interacting with its target protein (1EA1). Therefore, the title compound can be considered as an anti-*Candida* prodrug suitable for further investigations as a new antifungal candidate.

Acknowledgments: The authors would like to extend their sincere appreciation to the Deanship of Scientific Research at King Saud University for its funding of this research through the Research Group Project No. RGP-VPP-196.

Author Contributions: All authors discussed the contents of the manuscript and contributed to its preparation. Maha S. Almutairi, Ola A. Saleh and Mohamed I. Attia carried out the synthesis and characterization of the title molecule. Devarasu Manimaran and Issac Hubert Joe performed the computational work.

Conflict of Interests: The authors have declared that there are no conflict of interests.

References

1. Vanden-Bossche, H.; Dromer, F.; Improvisi, I.; Lozano-Chiu, M.; Rex, J.H.; Sanglards, D. Antifungal drug resistance in pathogenic fungi. *Med. Mycol.* **1998**, *36*, 119–128. [PubMed]
2. Odds, F.; Brown, A.J.P.; Gow, N.A.R. Antifungal agents: Mechanisms of action. *Trends Microbiol.* **2003**, *11*, 272–279. [CrossRef]
3. Hamdan, J.S.; Hahn, R.C. Antifungal drugs for systemic mycosis: An overview of mechanism of action and resistance. *Anti-Infect. Agents Med. Chem.* **2006**, *5*, 403–412. [CrossRef]
4. Almutairi, M.S.; Attia, M.I.; Ghabbour, H.A.; Ghoneim, S.W.; Abdel-Aziz, H.A.; Fun, H.-K. Crystal structure of ({(*E*)-[3-(1*H*-imidazol-1-yl)-1-phenylpropylidene]amino}oxy)(4-methylphenyl)-methanone, $C_{20}H_{19}N_3O_2$. *Z. Kristallogr. New Cryst. Struct.* **2014**, *229*, 307–308. [CrossRef]
5. Attia, M.I.; Zakaria, A.S.; Almutairi, M.S.; Ghoneim, S.W. *In Vitro* anti-*Candida* activity of certain new 3-(1*H*-imidazol-1-yl)propan-1-one oxime esters. *Molecules* **2013**, *18*, 12208–12221. [CrossRef] [PubMed]
6. Frisch, M.J.; Trucks, G.W.; Schlegel, H.B.; Scuseria, G.E.; Robb, M.A.; Cheeseman, J.R.; Scalmani, G.; Barone, V.; Mennucci, B.; Petersson, G.A.; *et al*. *Gaussian 09, Revision A.02*; Gaussian, Inc.: Wallingford, CT, USA, 2009.
7. Scott, A.P.; Radom, L. Harmonic vibrational frequencies: An evaluation of Hartree-Fock, Møller-Plesset, quadratic configuration interaction, density functional theory, and semiempirical scale factors. *J. Phys. Chem.* **1996**, *100*, 16502–16513. [CrossRef]
8. Foresman, J.B.; Frisch, A. *Exploring Chemistry with Electronic Structure Methods*; Gaussian Inc.: Pittsburgh, PA, USA, 1996.
9. Keresztury, G.; Chalmers, J.M.; Griffith, P.R. *Raman Spectroscopy: Theory in Handbook of Vibrational Spectroscopy*; John Wiley & Sons: New York, NY, USA, 2002.
10. Glendening, E.D.; Reed, A.E.; Carpenter, J.E.; Weinhold, F. *NBOi*; version 3.1; TCI, University of Wisconsin: Madison, WI, USA, 1998.
11. Glendening, E.D.; Reed, A.E.; Carpenter, J.E.; Weinhold, F. *NBO*; version 3.1; Theoretical Chemistry Institute and Department of Chemistry, University of Wisconsin: Madison, WI, USA, 1998.
12. Varsanyi, G. *Vibrational Spectra of Benzene Derivatives*; Academic Press: New York, NY, USA, 1969.
13. Jamroz, M.H. Vibrational Energy Distribution Analysis VEDA 4. Hindawi: Warsaw, Poland, 2004.
14. Socrates, G. *Infrared Characteristic Group Frequencies*; John Wiley & Sons: New York, NY, USA, 1980.
15. Smith, B.C. *Infrared Spectral Interpretation: A Systematic Approach*; CRC Press: New York, NY, USA, 1999.
16. Lin-Vein, D.; Colthup, N.B.; Fateley, W.G.; Grasselli, J.G. *The Handbook of Infrared and Raman Characteristic Frequencies of Organic Molecules*; Academic Press: New York, NY, USA, 1991.
17. Casado, J.; Hernandez, V.; Hotta, S.; Lopez Navarrete, J.T. Vibrational spectra of charged defects in a series of α,α'-dimethyl end-capped oligothiophenes induced by chemical doping with iodine. *J. Chem. Phys.* **1998**, *109*, 10419–10429. [CrossRef]
18. Gussoni, M. Infrared intensities: A new tool in chemistry. *J. Mol. Struct.* **1986**, *141*, 63–92. [CrossRef]
19. Bellamy, L.J. *The Infra-Red Spectra of Complex Molecules*; Chapman & Hall: London, UK, 1975.
20. Forsyth, D.A.; Sebag, A.B. Computed $^{13}C\cdot$ NMR chemical shifts via empirically scaled GIAO shieldings and molecular mechanics geometries. Conformation and configuration from ^{13}C shifts. *J. Am. Chem. Soc.* **1997**, *119*, 9483–9494. [CrossRef]
21. Rablen, P.R.; Pearlman, S.A.; Finkbiner, J. A comparison of density functional methods for the estimation of proton chemical shifts with chemical accuracy. *J. Phys. Chem. A* **1999**, *103*, 7357–7363. [CrossRef]
22. Costa, L.P.A.; de Albuquerque, C.F.; dos Santos, F.M.; de Amorim, M.B., Jr. GIAO-HDFT scaling factor for $^{13}C\cdot$ NMR chemical shifts calculation. *J. Phys. Org. Chem.* **2010**, *23*, 972–977.
23. Van Eikema-Hommes, N.J.R.; Clark, T. Regression formulae for *ab initio* and density functional calculated chemical shifts. *J. Mol. Model.* **2005**, *11*, 175–185. [CrossRef] [PubMed]
24. Jain, R.; Bally, T.; Rablen, P.R. Calculating accurate proton chemical shifts of organic molecules with density functional methods and modest basis sets. *J. Org. Chem.* **2009**, *74*, 4017–4023. [CrossRef] [PubMed]

25. Giesen, D.; Zumbulyadis, N. A hybrid quantum mechanical and empirical model for the prediction of isotropic ^{13}C shielding constants of organic molecules. *Phys. Chem. Chem. Phys.* **2002**, *4*, 5498–5507. [CrossRef]
26. Morris, G.M.; Huey, R.; Lindstrom, W.; Sanner, M.F.; Belew, R.K.; Goodsell, D.S.; Olson, A.J. AutoDock4 and AutoDockTools4: Automated docking with selective receptor flexibility. *J. Comput. Chem.* **2009**, *16*, 2785–2791. [CrossRef] [PubMed]
27. Podust, L.M.; Poulos, T.L.; Waterman, M.R. Crystal structure of cytochrome P450 14alpha-sterol demethylase (CYP51) from Mycobacterium tuberculosis in complex with azole inhibitors. *Proc. Natl. Acad. Sci. USA* **2001**, *98*, 3068–3073. [CrossRef] [PubMed]
28. Bernstein, F.C.; Koetzle, T.F.; Williams, G.J.; Meyer, E.E., Jr.; Brice, M.D.; Rodgers, J.R.; Kennard, O.; Shimanouchi, T.; Tasumi, M. The Protein Data Bank: A computer-based archival file for macromolecular structures. *J. Mol. Biol.* **1977**, *112*, 535–542. [CrossRef]
29. Morris, G.M.; Goodsell, D.S.; Halliday, R.S.; Huey, R.; Hart, W.E.; Belew, R.K.; Olson, A.J. Automated docking using a Lamarckian genetic algorithm and an empirical binding free energy function. *J. Comput. Chem.* **1998**, *19*, 1639–1662. [CrossRef]
30. Huey, R.; Morris, G.M.; Olson, A.J.; Goodsell, D.S. A semiempirical free energy force field with charge-based desolvation. *J. Comput. Chem.* **2007**, *28*, 1145–1152. [CrossRef] [PubMed]